

# Microscopic Origin of Universal Quasilinear Band Structures of Transparent Conducting Oxides

Youngho Kang,<sup>1</sup> Sang Ho Jeon,<sup>1</sup> Young-Woo Son,<sup>2</sup> Young-Su Lee,<sup>3</sup> Myungkwan Ryu,<sup>4</sup>  
Sangyoon Lee,<sup>4,\*</sup> and Seungwu Han<sup>1,†</sup>

<sup>1</sup>Department of Materials Science and Engineering, Seoul National University, Seoul 151-755, Korea

<sup>2</sup>Korea Institute for Advanced Study, Seoul 130-722, Korea

<sup>3</sup>Future Convergence Research Division, Korea Institute of Science and Technology, Seoul 136-791, Korea

<sup>4</sup>Samsung Advanced Institute of Technology, Samsung Electronics, Yongin, Gyeonggi-do 446-712, Korea

(Received 3 January 2012; published 11 May 2012)

A tight-binding-based microscopic theory is developed that accounts for quasilinear conduction bands appearing commonly in transparent conducting oxides. It is found that the interaction between oxygen  $p$  and metal  $s$  orbitals plays a critical role in determining the band structure around the conduction-band minimum. Under certain types of short-range orders, the tight-binding model universally leads to a dispersion relation which corresponds to that of the massive Dirac particle. The impact of the graphenelike band structure is demonstrated by evaluating the electron mobility of highly doped  $n$ -type ZnO.

DOI: 10.1103/PhysRevLett.108.196404

PACS numbers: 71.20.Nr, 31.15.aq, 71.23.Cq, 72.20.-i

Combining two opposing material properties of metallic conductivity and transparency of insulators, transparent conducting oxides (TCOs) such as ZnO,  $\text{In}_2\text{O}_3$ ,  $\text{SnO}_2$ , and their compound structures are widely used in various electronic, optical, and energy applications [1]. Most TCOs exhibit  $n$ -type conductivity with the electron mobility ranging over 10–100  $\text{cm}^2/\text{V} \cdot \text{s}$  which is exceptionally high among oxide families [2]. Recently, the transparent amorphous semiconducting oxides (TASOs) such as  $a$ - $\text{InGaZnO}$  have been receiving a good deal of attention as they enable flexible and transparent thin film transistors [3]. The electron mobility of the device was as high as  $\sim 10 \text{ cm}^2/\text{V} \cdot \text{s}$  which is comparable to typical crystalline materials. The high conductivity of TASOs is often understood by the large overlap between metal  $s$  orbitals [1,3].

On the theoretical side, the band structures of TCOs have been investigated at various computational levels [4,5]. It is intriguing that the conduction-band structures all look similar in spite of disparate atomic structures. We corroborate this point in Figs. 1(a)–1(c) which show band structures of ZnO,  $\text{In}_2\text{O}_3$ , and  $\text{Zn}_2\text{SnO}_4$  calculated around  $\Gamma$  point within the generalized gradient approximation [6] plus  $U(\text{GGA} + U)$  [7]. It is seen that all conduction bands have a single minimum at the  $\Gamma$  point and becomes linear at higher energies. The Fermi surfaces at the (electron) carrier density of  $10^{21} \text{ cm}^{-3}$  are almost spherical (see insets of the figures), indicating highly isotropic dispersion relations. Furthermore, the pseudoband structure of amorphous  $\text{In}_2\text{ZnO}_4$  ( $a$ - $\text{In}_2\text{ZnO}_4$ ) in Fig. 1(d) also displays a crystalline dispersion near the conduction bottom. (Similar observations were also noted in Refs. [9,10].) One may suspect that the apparent crystalline band of amorphous structures is an artifact arising from periodic boundary conditions imposed on the supercell calculations. To test this, we increased the supercell size for  $a$ - $\text{In}_2\text{ZnO}_4$  along a specific direction by two or three times and

confirmed that the band structure is well maintained. (See Supplemental Material Sec. 1 [11].) This implies that the apparent crystalline band in TASOs is an intrinsic property of the material and  $\vec{k}$  near the  $\Gamma$  point could be a good quantum number in spite of the long-range disorder. The dispersion relations in Fig. 1 are reminiscent of that of the massive Dirac particle in the form of  $E = \sqrt{\epsilon^2 + \gamma^2 k^2}$ .

The isotropy and universality in band structures of TCOs and TASOs have been largely understood by the overlap between cation  $s$  orbitals (see Ch. 2 of Ref. [1]).

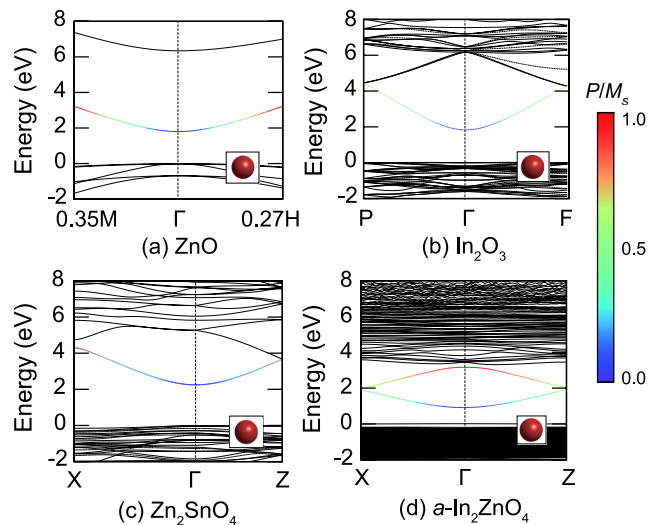


FIG. 1 (color online). Band structures of (a) ZnO, (b)  $\text{In}_2\text{O}_3$ , (c)  $\text{Zn}_2\text{SnO}_4$  (inverse-spinel), and (d)  $\text{In}_2\text{ZnO}_4$  (amorphous). The energy zero is set to the valence top. The color code in the lowest conduction bands indicate the weight of oxygen  $p$  orbitals ( $P$ ) normalized by that of metal  $s$  orbitals ( $M_s$ ). The inset spheres are Fermi surfaces at the nominal carrier density of  $10^{21}$  (crystalline) or  $10^{20}$  (amorphous)  $\text{cm}^{-3}$ .

This is based on the theoretical analysis that the conduction bottom is dominated by the metal  $s$  orbitals that are highly isotropic and the overlap integral between them is insensitive to the orientational disorder. In Fig. 1, we visualize the weight of oxygen  $p$  orbitals normalized by that of the metal  $s$  orbitals for the lowest conduction bands. Even though the contribution of oxygen  $p$  orbital is negligible right at the conduction bottom, it becomes progressively significant with increasing energy. Since the universality in band shapes persists up to these high-energy ranges, the argument based on the overlap between metal  $s$  orbitals cannot fully account for the universal band structure, which calls for a new microscopic theory. (The importance of oxygen  $p$  orbital was also noted in Ref. [4].) Motivated by the foregoing discussions, we propose in this Letter a tight-binding (TB) model which can apply to conduction bands of most TCOs and TASOs.

As the first step, we assume that conduction bands of TCOs and TASOs are well expanded by an orthonormal basis set similar to atomic orbitals,  $|s\rangle$ ,  $|w\rangle$ , and  $|p\rangle$ , each representing metal  $s$ , and oxygen  $s$  and  $p$  orbitals, respectively. The existence of such a basis set is in part supported by investigating the maximally localized Wannier functions (MLWFs) [12] for ZnO in the zinc blende structure (see Supplemental Material Sec. 2 [11]). For TB parameters, we consider only on-site terms, first-neighbor interactions between  $|s\rangle$  and  $|w\rangle$  or  $|p\rangle$ , and second-neighbor interactions between  $|s\rangle$ . The Kohn-Sham Hamiltonian matrix for ZnO constructed by MLWFs indicates that other terms are negligible.

To simplify the Hamiltonian matrix ( $\mathcal{H}$ ), we examined local configurations around metal and oxygen atoms in various crystalline and amorphous structures of TCOs and TASOs comprising In, Ga, Zn, Cd, and Sn atoms. (For example, see the first chapter of Ref. [1].) It is found that most of the local geometries around cations are close to tetrahedral or octahedral geometries as shown in Figs. 2(a) and 2(b), respectively, which is a result of the octet rule [13]. Under these highly symmetric local configurations, one can identify various mathematical conditions on  $\mathcal{H}$ ; in the case of metal atoms at the center of oxygen tetrahedra or octahedra, the following relation holds among the Hamiltonian matrix elements to the lowest order of  $|\vec{k}|$ :

$$\langle s | \mathcal{H} \sum_{j=1}^N e^{i\vec{k}\cdot\vec{d}_j} | p_{\hat{n},j} \rangle \simeq -i\gamma^s \vec{k} \cdot \hat{n}, \quad (1)$$

where  $N$  is the number of neighboring oxygen atoms,  $\vec{d}_j$  is the displacement vector from the center to the  $j$ th oxygen atom, and  $|p_{\hat{n},j}\rangle$  is its  $p$  orbital pointing to  $\hat{n}$ . In Eq. (1),  $\gamma^s$  is a parameter depending on the hopping integral for  $sp\sigma$  bonding. We call the relation in Eq. (1) ‘‘parallel’’ coupling. The corresponding relation between  $|s\rangle$  and  $|w\rangle$  orbitals is

$$\langle s | \mathcal{H} \sum_{j=1}^N e^{i\vec{k}\cdot\vec{d}_j} | w_j \rangle \simeq \alpha^s, \quad (2)$$

where  $\alpha^s$  is the parameter proportional to  $ss\sigma$  bonding between metal and oxygen  $s$  orbitals. This relation will be named ‘‘isotropic’’ coupling. The important property of parallel and isotropic coupling is that they do not depend on the orientation of oxygen polyhedra.

On the other hand, the cations surrounding an oxygen atom mostly form the tetrahedral geometry. (Triangular structures can appear when Sn atoms are abundant; see below.) In the case of the tetrahedral configuration, similar relations as above can be derived for  $|w\rangle$  and  $|p\rangle$  (for simplicity, we assume that all neighboring cations are of the same species at the moment):

$$\langle p_{\hat{n}} | \mathcal{H} \sum_{j=1}^N e^{i\vec{k}\cdot\vec{d}_j} | s_j \rangle \simeq i\gamma^p \vec{k} \cdot \hat{n}, \quad (3)$$

$$\langle w | \mathcal{H} \sum_{j=1}^N e^{i\vec{k}\cdot\vec{d}_j} | s_j \rangle \simeq \alpha^w, \quad (4)$$

where  $j$  runs over neighboring cations. Because of the high-coordination numbers, we assume the isotropic coupling between  $|s\rangle$ 's with the coupling constant of  $\beta$  [14].

Under the above conditions of parallel and isotropic coupling, one can obtain the eigenstates and eigenvectors in an analytic way. For now, we consider only binary oxides and assume that  $\gamma^{s(p)}$  and  $\alpha^{s(w)}$  are uniform throughout the material. However, the formulation is not limited to crystalline structures but also applicable to amorphous materials as long as the short-range order assumes one of those in Fig. 2. We first construct Bloch-like propagating states that linearly combine all orbitals in the system with the phase factor propagating along a  $\vec{k}$  vector:  $|S_{\vec{k}}\rangle = \sqrt{1/q} \sum_{j=1}^q e^{i\vec{k}\cdot\vec{d}_j} |s_j\rangle$ ,  $|P_{\hat{n},\vec{k}}\rangle = \sqrt{1/r} \sum_{j=1}^r e^{i\vec{k}\cdot\vec{d}_j} |p_{\hat{n},j}\rangle$ , and  $|W_{\vec{k}}\rangle = \sqrt{1/r} \sum_{j=1}^r e^{i\vec{k}\cdot\vec{d}_j} |w_j\rangle$ , where  $q$  and  $r$  are numbers of cations and anions in the whole system, respectively. Note that the orthonormality is maintained between states with different types and/or  $\vec{k}$ 's.

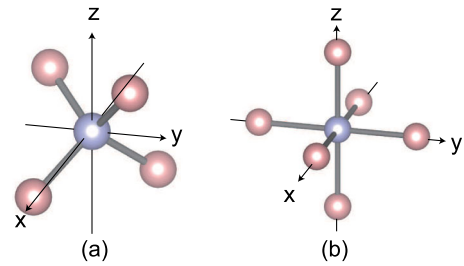


FIG. 2 (color online). Schematic pictures of the local geometry around metal and oxygen atoms in TCOs and TASOs. (a) Tetrahedral and (b) octahedral geometries.

Next, we consider their linear combination with undetermined coefficients  $\{c_i\}$ :

$$|\Psi_{\vec{k}}\rangle = c_1|S_{\vec{k}}\rangle + c_2|W_{\vec{k}}\rangle + c_3|P_{x,\vec{k}}\rangle + c_4|P_{y,\vec{k}}\rangle + c_5|P_{z,\vec{k}}\rangle. \quad (5)$$

Owing to above parallel and isotropic coupling,  $\mathcal{H}|\Psi_{\vec{k}}\rangle$  can be expressed as a linear combination of the five Bloch-like states. This leads to the following  $5 \times 5$  Hamiltonian matrix:

$$\mathcal{H} = \begin{pmatrix} \epsilon^s + \beta & \alpha & -i\gamma k_x & -i\gamma k_y & -i\gamma k_z \\ \alpha & \epsilon^w & 0 & 0 & 0 \\ i\gamma k_x & 0 & \epsilon^p & 0 & 0 \\ i\gamma k_y & 0 & 0 & \epsilon^p & 0 \\ i\gamma k_z & 0 & 0 & 0 & \epsilon^p \end{pmatrix}, \quad (6)$$

where  $\epsilon^{s,w,p}$  indicate the on-site energy of each basis,  $\alpha = \sqrt{\frac{q}{r}}\alpha^s = \sqrt{\frac{r}{q}}\alpha^w$ , and  $\gamma = \sqrt{\frac{q}{r}}\gamma^s = \sqrt{\frac{r}{q}}\gamma^p$ . Furthermore, because of the strong  $\sigma$  interaction between  $|s\rangle$  and  $|w\rangle$ , the conduction bands consist of antibonding states of  $|S_{\vec{k}}\rangle$  and  $|W_{\vec{k}}\rangle$  with relative coefficients almost constant. As such, we consider only the higher-energy state,  $|\Sigma_{\vec{k}}\rangle = \cos\phi|S_{\vec{k}}\rangle - \sin\phi|W_{\vec{k}}\rangle$  ( $0 < \phi < \frac{\pi}{2}$ ), which is obtained by diagonalizing  $2 \times 2$  submatrix in the upper left corner of Eq. (6). This effectively reduces the Hamiltonian to the following  $4 \times 4$  matrix:

$$\begin{pmatrix} \epsilon & -i\tilde{\gamma}k_x & -i\tilde{\gamma}k_y & -i\tilde{\gamma}k_z \\ i\tilde{\gamma}k_x & -\epsilon & 0 & 0 \\ i\tilde{\gamma}k_y & 0 & -\epsilon & 0 \\ i\tilde{\gamma}k_z & 0 & 0 & -\epsilon \end{pmatrix}, \quad (7)$$

where  $\tilde{\gamma} = \gamma \cos\phi$  and the on-site energies are shifted to simplify the diagonal components. We note that a similar Hamiltonian was identified in the topologically trivial insulator  $\text{CoSb}_3$  [15]. The three lowest eigenstates and eigenvalues of Eq. (7) correspond to the valence band, which is not of concern here. The highest eigenvalue and eigenstate for the conduction band are given as follows:

$$E = \sqrt{\epsilon^2 + \tilde{\gamma}^2 k^2} \quad (8)$$

$$|\Psi_{\vec{k}}\rangle = \sqrt{\frac{\lambda_1}{\lambda_1 + \lambda_2}}|\Sigma_{\vec{k}}\rangle + i\sqrt{\frac{\lambda_2}{\lambda_1 + \lambda_2}}|P_{\vec{k},\vec{k}}\rangle, \quad (9)$$

where  $\lambda_1 = \sqrt{\epsilon^2 + \tilde{\gamma}^2 k^2} + \epsilon$  and  $\lambda_2 = \sqrt{\epsilon^2 + \tilde{\gamma}^2 k^2} - \epsilon$ . Equation (8) is indeed the dispersion relation of the massive Dirac particles as was hinted in the introduction. One important property of the eigenfunction in Eq. (9) is that oxygen  $p$  orbitals are always parallel to  $\vec{k}$ , which is a consequence of the isotropic coupling. This will be confirmed by the first-principles results below.

For multicomponent TCOs or TASOs, the oxygen atoms can be surrounded by different metal species. The applicability of the above approach critically depends on the degree of variations in the TB parameters, particularly those between  $|s\rangle$  and  $|p\rangle$ . We compared this parameter among Zn-O, In-O, and Sn-O by examining the band structures of binary phases and it is found that the variation is  $\sim 10\%$ . Therefore, the above TB approach may also play as a reasonable approximation in the multicomponent structures.

Next, we compare the TB results with the first-principles calculations. As a reference system, we choose ZnO in the zinc-blende structure but the same conclusions can be drawn for wurtzite ZnO. The discrete symbols in Fig. 3(a) show the conduction bands along different  $\vec{k}$  directions. The solid line in the same figure is a fitted curve with the form of  $E = \epsilon_0 + \sqrt{\epsilon^2 + \tilde{\gamma}^2 k^2}$  with parameters of  $\epsilon_0 = 1.55$  eV,  $\epsilon = 0.86$  eV, and  $\tilde{\gamma}/\hbar = 8.50 \times 10^5$  m/s. The good agreement between first-principles and TB energies can be seen up to the nominal carrier density of  $10^{21}$   $\text{cm}^{-3}$ .

Equation (9) also implies that the oxygen  $p$  orbitals are always parallel to the  $\vec{k}$  vector. This is confirmed in Fig. 3(b) which shows that the local projection to the oxygen  $p$  orbitals orthogonal to  $\vec{k}$  is negligible (see  $|P_{\perp}/M_s\rangle$ ). In contrast, the relative weight of oxygen  $p$  orbitals pointing

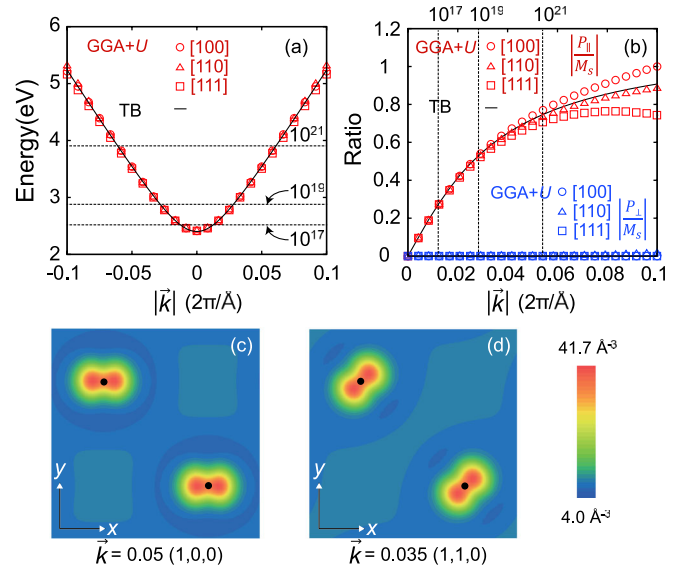


FIG. 3 (color online). (a) Conduction bands of cubic ZnO along various  $\vec{k}$  directions. The solid line is the fitted dispersion relation. The Fermi levels at 0 K corresponding to various (electron) carrier densities ( $\text{cm}^{-3}$ ) are indicated by dashed horizontal lines. The consideration of finite-temperature Fermi-Dirac distributions shifts down the Fermi level slightly ( $\sim 0.01$  eV at 300 K). (b) The relative ratio of oxygen  $p$  orbitals parallel or perpendicular to  $\vec{k}$  ( $|P_{\parallel}/M_s|$  and  $|P_{\perp}/M_s|$ , respectively). The solid line indicates the result with parameters fitted in (a). (c) and (d) show the square of wave functions at specific  $\vec{k}$  points. The black dots indicate oxygen atoms.

along  $\vec{k}(|P_{\parallel}/M_S|)$  is in good accordance with  $\sqrt{\lambda_2/\lambda_1}$  with the above values of  $\epsilon$  and  $\tilde{\gamma}$ . (A scaling factor of 1.16 is multiplied.) Figures 3(c) and 3(d) confirm the parallel relation more directly. In addition, the eigenstate in Eq. (9) indicates that the ratio between coefficients of  $|\Sigma_{\vec{k}}\rangle$  and  $|P_{\vec{k},\vec{k}}\rangle$  is pure imaginary, and this is also confirmed by examining the phase relation among orbital projections of a specific state.

Good agreement is found for every crystalline and amorphous structure that we examined (see Supplemental Material Sec. 3 [11]) although  $|P_{\perp}/M_S|$  is not negligible in some materials due to deviation from the ideal geometries in Fig. 2. The distortion might be exacerbated in amorphous structures by the unrealistic quenching speed. For  $\text{SnO}_2$ , the oxygen atoms are surrounded by the triangular coordination of cations and obey a slightly modified form of the isotropic coupling. Nevertheless, the band structures and eigenfunctions are well described by the present tight-binding model. (There is, however, a biaxial character [16] from the distorted octahedra as shown in Supplemental Material Sec. 3 [11].)

To examine the impact of graphenelike band structures on the transport property, we investigate the electron mobility of single crystalline ZnO. In particular, we focus on the dependence on the carrier density since the band structure becomes markedly linear at high carrier densities. There are several scattering mechanisms that limit the electron mobility in single crystals [17]. Among them, it has been shown that the polar optical phonon (POP) and ionized impurity (II) scattering mechanisms dominate in ZnO [18]. (Our own calculation with free-electron model also confirms this.) Therefore, we consider these two scattering mechanisms in the following. For the model of II scattering, we employ the Brooks-Herring model but evaluate the density of carriers screening the impurity based on the density of states that results from Eq. (8).

In applying the Fermi golden rule to evaluating the scattering rate for each mechanism, the overlap integral between periodic parts of incoming and outgoing Bloch states are typically set to one [17]. In TCOs, however, the prefactor critically depends on the energy and scattering angle when the full quasilinear band structure is considered. This is confirmed in Fig. 4(a) which shows that the overlap integral for the elastic scattering mechanism is significantly reduced at high energies and large scattering angles. This is akin to the suppression of backward scattering in graphene [19] and is a result of chiral symmetry characteristic of the linear band. The rest of the computational details are based on the first-order Born approximation that is well developed in semiconductor theory [17] with parameters used in [18].

The mobility is evaluated from the low-field solution of Boltzmann transport equation in which the total scattering time ( $\tau$ ) is obtained by Mathiessen's rule,  $1/\tau = 1/\tau_{\text{POP}} + 1/\tau_{\text{II}}$  [20]. Figure 4(b) displays the total drift mobility and

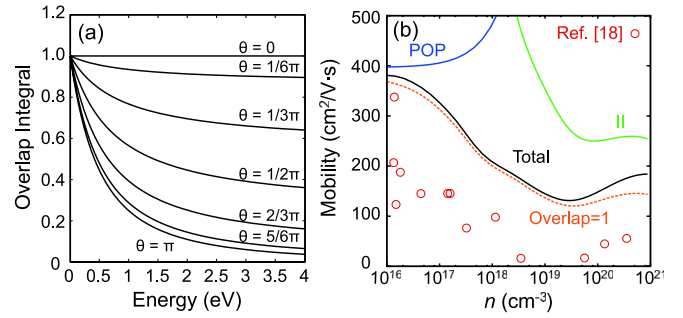


FIG. 4 (color online). (a) The overlap integral between the lattice-periodic parts of eigenfunctions with respect to the scattering angle and electron energy. The elastic scattering is assumed. (b) The computed total drift mobility of electrons in ZnO with respect to carrier densities. The circles are experimental data in Ref. [18]. The apparent divergence of individual mobility at  $10^{18} \text{ cm}^{-3}$  is due to the linear scale; the mobility is always finite.

individual contributions evaluated at 300 K. We note that the finite-temperature Fermi-Dirac distribution is used for the calculation. It is shown that POP and II scattering dominate in the low and high carrier density regions, respectively. The experimental data on the epitaxial film of Ga-doped ZnO are also marked as circles [18]. It is seen that the theoretical values are bigger than the experimental data consistently by  $\sim 100 \text{ cm}^2/\text{V}\cdot\text{s}$ . This might be due to the first-order Born approximation which tends to overestimate the electron mobility. Considering higher order terms and multiple scattering, the electron mobility is likely to be lowered, but further investigation is beyond the present scope [21]. Nevertheless, the overall dependence is in good agreement with experiment. In particular, the carrier density showing the minimum mobility agrees well between theory and experiment ( $\sim 10^{19} \text{ cm}^{-3}$ ). We note that the previous model assumed in Ref. [18] was not able to reproduce the minimum mobility. The fact that the upshift occurs at high carrier densities hints that the suppressed backscattering in Fig. 4(a) contributes to this. To verify this, the mobility is recalculated in Fig. 4(b) with the overlap part set to one (see the dashed line). It can be seen that the upshift is significantly suppressed, underscoring the importance of the angle-dependent overlap integral which is characteristic of the graphenelike band structure.

It is noted that quasilinear band structures can be observed in other materials such as Si and GaAs over a certain  $\vec{k}$ -space region. However, we stress that the uniqueness in TCOs is that the dispersion relation is insensitive to the medium- and long-range orders due to the parallel and isotropic coupling conditions. This does not hold for other classes of materials which require a perfect tetrahedral ordering throughout the whole crystal for the existence of quasilinear bands.

In summary, we provided a TB-based microscopic theory that addresses the universality in conduction-band shapes of TCOs and TASOs. Under certain types of short-range orders, the matrix elements satisfies the

parallel and isotropic coupling relations, which leads to the universal dispersion relation similar to that of the massive Dirac particle, even in amorphous structures. The impact of the graphenelike band structure was demonstrated by evaluating the electron mobility of highly doped ZnO. The quasilinear band structure should be critical in the low-dimensional system such as surfaces and interfaces. In this respect, 2DEG appearing in the MgZnO/ZnO heterostructure is particularly interesting [22]. Last, we note that the present analysis and conclusions are relevant for  $n$ -type TCOs, not for  $p$ -type ones.

This work was supported by the Center for Multiscale Energy System and the Quantum Metamaterials Research Center. The computations were carried out at KISTI (No. KSC-2010-C2-0010). We appreciate critical comments by Yong-Sung Kim.

---

\*sangyoon.lee@samsung.com

†hansw@snu.ac.kr

- [1] *Handbook of Transparent Conductors*, edited by D. S. Ginley (Springer, New York, 2011).
- [2] S. Calnan and A. N. Tiwari, *Thin Solid Films* **518**, 1839 (2010).
- [3] K. Nomura, H. Ohta, A. Takagi, T. Kamiya, M. Hirano, and H. Hosono, *Nature (London)* **432**, 488 (2004).
- [4] J. E. Medvedeva and C. L. Hettiarachchi, *Phys. Rev. B* **81**, 125116 (2010).
- [5] M. Usuda, N. Hamada, T. Kotani, and M. van Schilfhaarde, *Phys. Rev. B* **66**, 125101 (2002).
- [6] J. P. Perdew, K. Burke, and M. Ernzerhof, *Phys. Rev. Lett.* **77**, 3865 (1996).
- [7] All computations in this work were carried out by the Vienna *ab initio* simulation package [8]. The cutoff energy of 500 eV is used and  $\vec{k}$ -point convergence was carefully checked to ensure the energy convergence within 10 meV/atom. The structures are relaxed until the forces were converged to 0.02 eV/Å.  $U - J$  values in GGA +  $U$  calculations are set to 7, 7.5, and 3.5 eV for In  $4d$ , Zn  $3d$ , and Sn  $4d$ , respectively. The amorphous structure was generated by cooling the liquid at 2500 K with the quenching rate of  $-50$  K/ps down to 0 K followed by the full structural relaxation.
- [8] G. Kresse and J. Furthmüller, *Phys. Rev. B* **54**, 11 169 (1996); P. E. Blöchl, *Phys. Rev. B* **50**, 17 953 (1994).
- [9] J. Rosen and O. Warschkow, *Phys. Rev. B* **80**, 115215 (2009).
- [10] A. Walsh, J. L. F. Da Silva, and S. H. Wei, *Chem. Mater.* **21**, 5119 (2009).
- [11] See Supplemental Material at <http://link.aps.org/supplemental/10.1103/PhysRevLett.108.196404> for detailed information.
- [12] I. Souza, N. Marzari, and D. Vanderbilt, *Phys. Rev. B* **65**, 035109 (2001).
- [13] J. L. F. Da Silva, Y. Yan, and S. H. Wei, *Phys. Rev. Lett.* **100**, 255501 (2008).
- [14] The accuracy of Eqs. (1)–(4) was assessed by comparing with the numerical evaluation of left-hand sides, and the relative error was found to be less than 10% up to  $|\vec{k}|$  of  $0.05(2\pi/\text{Å})$  which corresponds to the carrier density of  $10^{21} \text{ cm}^{-3}$ .
- [15] J. C. Smith, S. Banerjee, V. Pardo, and W. E. Pickett, *Phys. Rev. Lett.* **106**, 056401 (2011).
- [16] R. Saniz, H. Dixit, D. Lamoën, and B. Partoens, *Appl. Phys. Lett.* **97**, 261901 (2010).
- [17] B. K. Ridley, *Quantum Process in Semiconductors* (Oxford University Press, New York, 1993), 3rd ed.
- [18] T. Makino, Y. Segawa, A. Tsukazaki, A. Ohtomo, and M. Kawasaki, *Appl. Phys. Lett.* **87**, 022101 (2005).
- [19] H. Suzuura and T. Ando, *Phys. Rev. Lett.* **89**, 266603 (2002).
- [20] M. V. Fischetti and S. E. Laux, *J. Appl. Phys.* **80**, 2234 (1996).
- [21] D. Chattopadhyay and H. J. Queisser, *Rev. Mod. Phys.* **53**, 745 (1981).
- [22] A. Tsukazaki, S. Akasaka, K. Nakahara, Y. Ohno, H. Ohno, D. Maryenko, A. Ohtomo, and M. Kawasaki, *Nature Mater.* **9**, 889 (2010).